*Progress In Electromagnetics Research M, Vol. 67, 105–117, 2018*

# Design of Grounding Grid Conductor Positioning Device on the Magnetic Field Method

**Xiaokuo Kou[1], Manling Dong[1], Fan Yang[2], Sheng Han[2, *], Ke Zhang[1], Lei Guo[1], and Guojun Ding[1]**

**Abstract**—The location and topology of grounding grid conductors are necessary to corrosion diagnosis and digging in most cases. In this paper, an integrated detecting device for grounding conductor buried position is designed. Based on the principle of magnetic field method, a multi-layer cascade PCB hollow coil sensor is designed. AC excitation current source, 16-channel control circuit, lock-in amplifier (LIA) circuit and 4-channel synchronous acquisition circuit are realized. The experimental test is completed for the integrated detection device, and results verify the feasibility of the system.

## 1. INTRODUCTION

As an important part of a power grounding system, grounding grid mainly exists in power plants and substations. It can be used for discharging large current rapidly, such as lightning current and fault current, which can reduce the rise of ground potential to protect the staff and device in the field. Many substations in the world are using carbon steel or galvanized flat steel as a grounding material due to the limitation of resource, economic and technical conditions [1]. After a long period of operation, the metals will be corroded in the soil, which directly reduces the security of the power system [2]. On some serious occasions, the conductor will fracture due to the corrosion and increase the ground resistance greatly, which will threaten the safety of electrical devices and staff in substations [3].

There are some common methods used to evaluate grounding systems, such as conduction-verification with current injection, visual inspection, and grounding resistance test [4]. The most common device to test the grounding grid is Smart Ground Meter in America. Many engineers use software such as CDEGS to assess existing grounding grid according to its construction drawings [5]. At the same time, new calculation models [6, 7] and analytical methods [8–10] are proposed, but most of them rely upon the position of the conductor.

In this paper, a positioning device for grounding grid is designed based on previous researches [11, 12]. The magnetic sensor module with multi-layer cascade PCB hollow coil is designed based on the analysis of target signal strength, EMI (Electromagnetic Compatibility) and existing measurement method. An array with $8 \times 2$ sensors is built to measure the target magnetic field distribution produced by the AC excitation current source designed with AD9833.

Considering the range of the target magnetic field and measurement efficiency, a 16-channel control circuit and a 4-channel synchronous acquisition circuit are designed. In order to filter out the odd harmonics and other interference signals, the circuit of the LIA is adopted

*Received 2 February 2018, Accepted 21 March 2018, Scheduled 11 April 2018*

* Corresponding author: Sheng Han (dashuiweng@gmail.com).

[1] State Grid Henan Electric Power Corporation Research Institute, Zhengzhou, Henan 450052, China. [2] Chongqing University, Chongqing 400044, China.

## 2. MAGNETIC FIELD METHOD

Magnetic Field Method injects current into the grounding grid and locate conductors based on magnetic information. The simplified structure of the grounding grid is shown in Fig. 1.

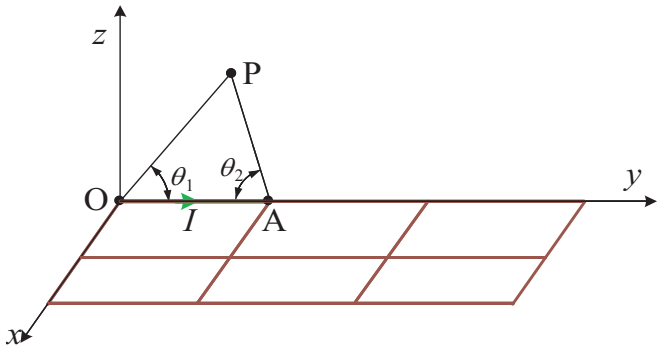


**Figure 1.** Calculation model of grounding grid.

In Fig. 1, the space magnetic field is calculated according to the superposition principle. Take the conductor $OA$ with length $L$ as an example, which carries current $I$. According to *Biot-Savart* law, the magnetic flux density $\mathbf{B}$ at point $P(x_p y_p z_p)$ can be obtained as follows:

$$\mathbf{B} = \frac{\mu I}{4\pi\rho}(\cos\theta_1 + \cos\theta_2)\mathbf{e}_\varphi \tag{1}$$

where,

$$\cos\theta_1 = \frac{y_p}{\sqrt{x_p^2 + y_p^2 + z_p^2}} \quad \cos\theta_2 = \frac{L - y_p}{\sqrt{x_p^2 + (L - y_p)^2 + Z_P^2}} \tag{2}$$

Assume that $I = 1\,\text{A}$, $L = 5\,\text{m}$, $x_p$ is the variable, take $y_p = 0$, $0.5\,\text{m}$, $1.5\,\text{m}$, $2.5\,\text{m}$, $z_p = 0.5\,\text{m}$. The curve of magnetic flux density $B_x(x)$ with position is shown in Fig. 2. There is an obvious peak character in the figure, directly above the conductor. With this feature, the exact position of conductor can be obtained. Curves in Fig. 2 represent different measurement paths.

A ground grid model with $120\,\text{m} \times 120\,\text{m}$ similar to Fig. 1 is built, with each mesh $10\,\text{m}$ long and buried depth $1\,\text{m}$, which is close to the real fact. A sinusoidal excitation current of $1\,\text{A}$, $1\,\text{kHz}$ is injected in the accessible node $N$ ($30\,\text{m}$, $0\,\text{m}$) and outflows from node $M$ ($30\,\text{m}$, $90\,\text{m}$).

The current will excite an magnetic signal at the same frequency above the ground. Take $|B_x|$ as an example and carry out the calculation. The distribution of magnetic flux density in the plane $1\,\text{m}$ above the conductors is shown in Fig. 3, and Fig. 4 shows the section curve at $y = 40\,\text{m}$.

Based on the simulation above, the target magnetic signal has following characters:

1) For a conductor parallel to the *x-axis*, its $|B_y|$ has a peak character; for a conductor parallel to the *y-axis*, $|B_x|$ has a peak character.
2) Each peak corresponds to a conductor below it. In addition, it is reliable to determine the buried position of grounding grid conductors.
3) The magnetic flux density on the ground above the grid conductors is $10^{-9} \sim 10^{-7}\,\text{T}$, when the injected excitation current is $1\,\text{A}$.

## 3. DESIGN OF MAGNETIC SENSOR

### 3.1. Measuring Principle

As shown in Fig. 5, an AC excitation current $i = I\sin(2\pi f_c \cdot t)$ is injected into node $M$ and extracted from $N$. Place the designed magnetic field measurement coil over conductors. The magnitude of the

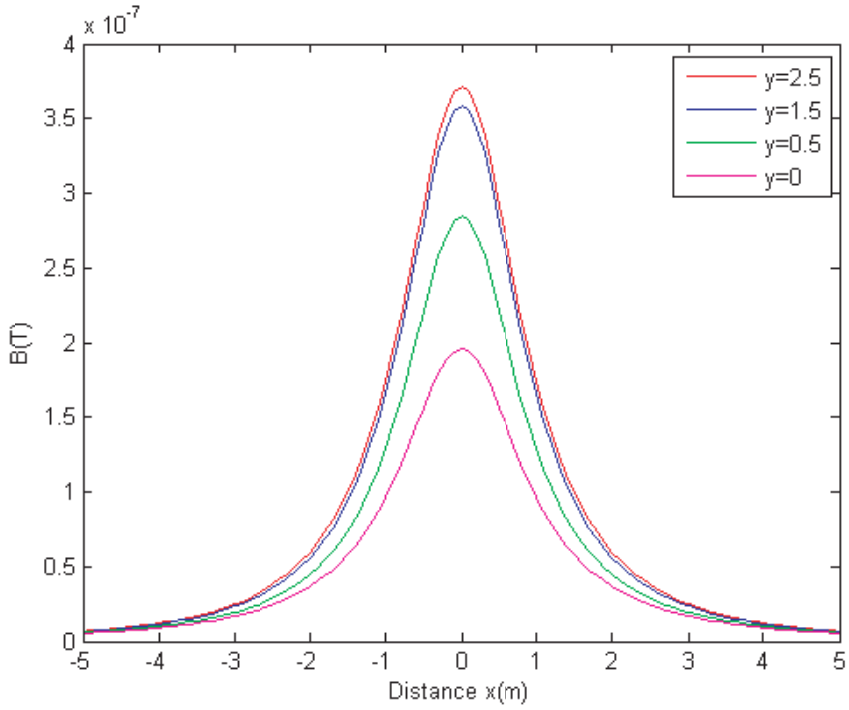


**Figure 2.** The curve of $B_x(x)$.

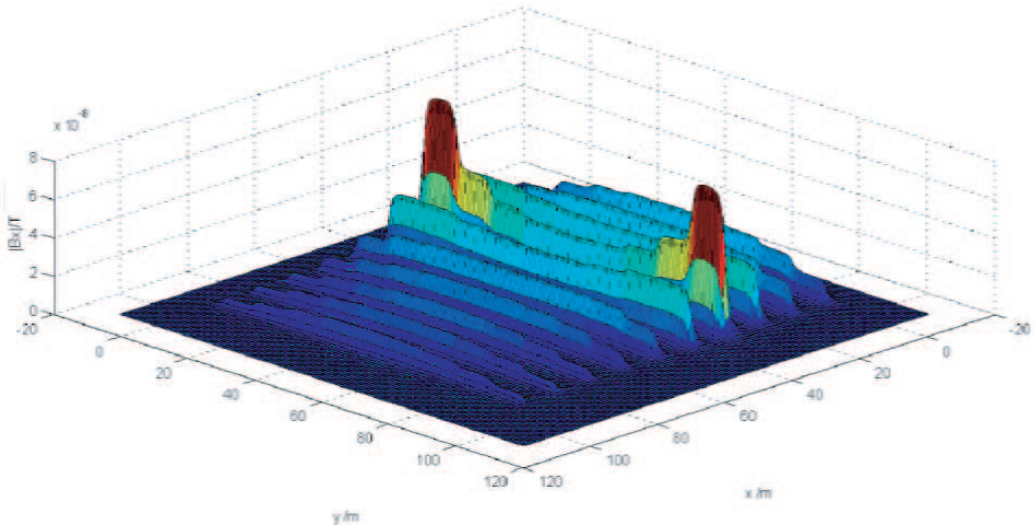

**Figure 3.** $|B_x|$ above the ground.

induced magnetic field is denoted by $B$. The angle between the coil and the direction of the magnetic field is $\theta$.

In this case, the effective magnetic flux passing through the coil is $\Psi$

$$\Psi = NSB\cos\theta \tag{3}$$

The induced electromotive force in the detecting coil is $E$

$$E = \frac{d\psi}{dt} = 2\pi f_c NSB_m \tag{4}$$

Connect the coil with a band-pass filter amplifier with the gain $A$. The output of the induced voltage

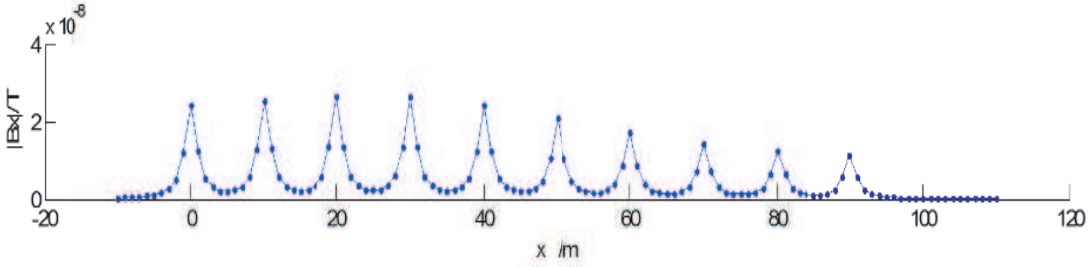


**Figure 4.** Distribution on the ground at $y = 40\,\text{m}$.

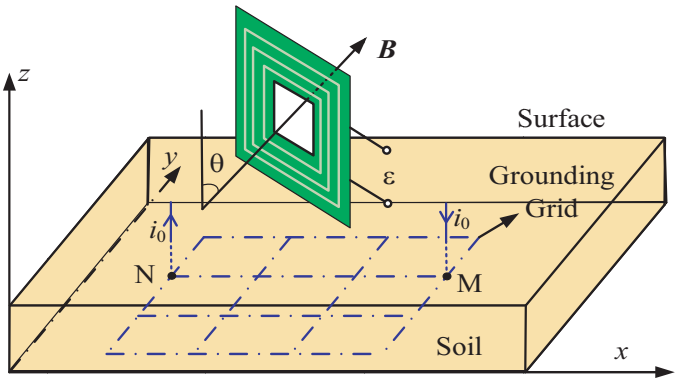


**Figure 5.** Schematic diagram of measurement.

is $V_o$

$$V_o = AE = 2\pi A f_c N S B_m \tag{5}$$

Signal $V_o$ has a linear relationship with induced magnetic field $B$, which is same frequency $f_c$. Therefore, it is feasible to measure the magnitude of the magnetic field indirectly by measuring $V_o$.

### 3.2. Physical Design

The structure of multilayer PCB hollow coils is adopted by the device in the magnetic sensor [13, 14]. Fig. 6 shows the structure of each coil. The wires between the upper and next layers are connected to

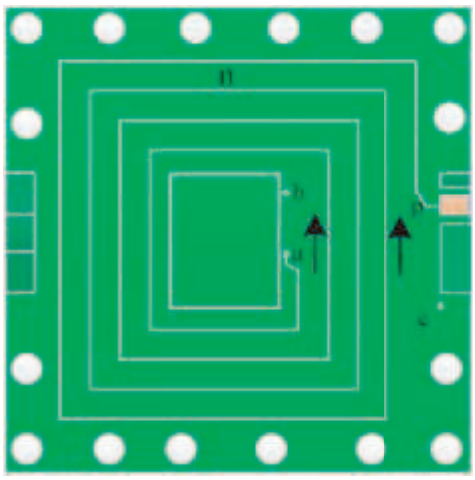

**Figure 6.** The structure of PCB coil.

each other through via holes so as to ensure that the coils are winded in the same direction. The pads are reserved as a signal output terminal on the top and bottom layers of the coil which are in a serrated protrusion so that the coils can be cascaded. The wiring of each layer is in parallel from top to bottom to avoid eddy currents between different layers. Through holes at the edge can be used to fix the PCB, or to make an external wire through if necessary.

Let the rectangular hollow sides of the coil be $L_1$ and $L_2$ respectively, and the number of windings of the single-layer coil is $n$. The effective area of the whole coil is $S = L_1 L_2$, and the effective number of turns $N = 4n + 0.5$.

To improve the anti-interference ability of the sensors, the PCB shields on the top and bottom layers of the coil were designed which are both grounded to make sure the magnetic circuit only passes through the hollow part of the coil during measurement. The top measurement coil is connected to an input terminal of the filter amplifying circuit as the reference ground for the signal output while the bottom measurement coil is connected to another input terminal of the filter amplifying circuit. Fig. 7 shows the combination of sensor and LIA.

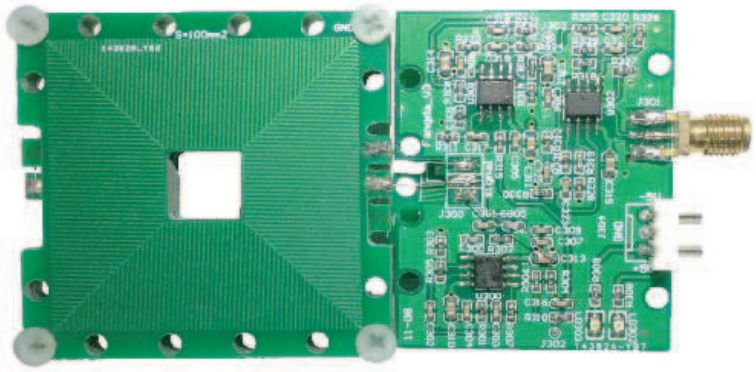

**Figure 7.** PCB hollow coil and its amplification filter circuit.

### 3.3. Magnetic Field Measurement Sensor Performance Test

Fig. 8 and Fig. 9 illustrate the schematic diagram and experiment setup. Use the standard AC excitation source XJ-IIB to inject an AC current of 1 A, 1 kHz into a circular current-carrying circuit. LIA chip AD630 also sets this current as the reference signal. The sensor is made up of cascade rectangular hollow coils of a four 4-layer PCB. The output of the coil is connected in turn to a band-pass filter circuit, a LIA circuit and an oscilloscope.

During the test, the PCB coils are parallel to the circular current-carrying loops, and their central axes coincide. In other words, the coil is used to measure the magnetic flux density on the axis of the

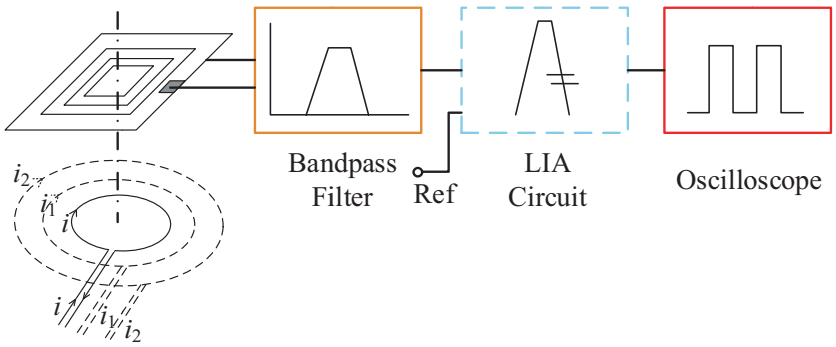


**Figure 8.** Schematic diagram of sensors test.

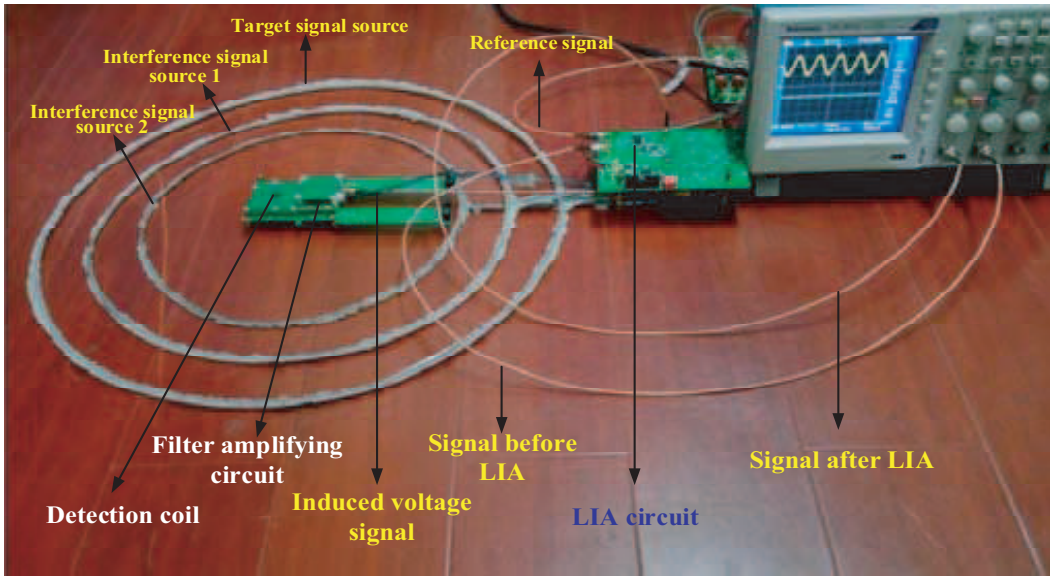


**Figure 9.** Anti-interference ability test.

current loop. The amplitude of the induced voltage is recorded by an oscilloscope. Change the radius of the circular current-carrying loop $a$. The magnetic field is calculated by the induced voltage and compared with the theoretical value, which verifies the accuracy of the data measured by the magnetic field sensor.

According to the theory of electromagnetic field, we can calculate the magnetic flux density $\mathbf{B}$ of a circular current carrying circuit on the central axis

$$\mathbf{B}_m = \frac{\mu_0 \mathbf{I}}{2a} \tag{6}$$

When the radius of the circular current-carrying loop is much larger than the size of the coil, it can be approximated that the sensor measures the magnitude of the magnetic flux density $\mathbf{B}$ on the axis in the center.

The parameters of the magnetic field measurement sensor in the test are as follows:

The area of the coil is $S = 10\,\text{mm} \times 10\,\text{mm}$. The number of turns of each PCB is $N = 192.5$. The passband gain of the band pass filter is $A = 400$, and its center frequency is $f = 1\,\text{kHz}$, with a passband range of 500 Hz to 1700 Hz. Substituting into Eq. (5)

$$v_{om} = kB_m = \frac{k\mu_0 I}{2a} = \frac{1.94 \times 10^5 \times 4\pi \times 10^{-7}}{2a} \tag{7}$$

The circular current-carrying loops of different sizes are adopted in the test, respectively. Test the circular current-carrying loops of different radii $a$. In the case of no phase-locked amplifier circuit, the sensor induced voltage waveform and effective value are recorded by an oscilloscope, and compared with the theoretical value. The theoretical value assumes that the magnetic field is evenly distributed in the loop. The results are shown in Table 1.

Then, increase the LIA circuit for anti-jamming test. Inject the current of 1 A, 1 kHz into the loop of $a = 25\,\text{cm}$, and measure the magnetic field intensity on the central axis. In addition, place two loops with smaller radius and carry current of different frequencies, inside the former loop. The two smaller loops can be used as an interference source. If no interference source is set, the measured reference value is 0.048 V.

Change the current magnitude and frequency of the interfering signal source, and the measurement results are shown in Table 2 below.

In the table, group 1 is focused on the power frequency interference, and it is the strongest in the substation. Group 2 and group 3 are used to test the anti-interference ability with 800 Hz, which is

**Table 1.** The results of sensor test.

| | Radius of circular current-carrying circuit $a$ (cm) | | | | |
|---|---|---|---|---|---|
| | 5 | 10 | 15 | 20 | 25 |
| Theoretical magnetic intensity $B(\mu T)$ | 12.6 | 6.28 | 4.19 | 3.15 | 2.51 |
| Theoretical induced voltage $v_{om}$ (V) | 2.44 | 1.22 | 0.813 | 0.609 | 0.488 |
| Measured induced voltage (V) | 2.24 | 1.12 | 0.800 | 0.600 | 0.480 |
| Error (%) | 8.20 | 8.20 | 1.60 | 1.48 | 1.64 |

**Table 2.** Experimental projects and results.

| Signal Type | | B/μT | $f$/Hz | Value/V | Error/% |
|---|---|---|---|---|---|
| Target Signal | | 0.251 | 1000 | 0.048 | —— |
| Interference Signal Group 1 | Interference 1 | 20 | 50 | 0.044 | 8.33% |
| | Interference 2 | 4.19 | 1500 | | |
| Interference Signal Group 2 | Interference 1 | 4.19 | 800 | 0.046 | 4.17% |
| | Interference 2 | 6.28 | 1500 | | |
| Interference Signal Group 3 | Interference 1 | 6.28 | 800 | 0.045 | 6.25% |
| | Interference 2 | 12.6 | 1500 | | |

close to the target signal. Interference 2 is used to simulate the high-frequency interference. The results show that the error of magnetic field measurement is less than 10%, weather the interference is much stronger than target signal.

## 4. MEASUREMENT DEVICE

The structure of grounding grid conductor positioning device is shown in Fig. 10. The AC excitation current source module is connected to two attainable nodes, and the current can be injected into the grid through wire and clamps. Subsequently, the induced magnetic field appears at the ground surface.

The original induction magnetic field signal is converted to the collectable signal by the coils and data acquisition chip. The signal processing circuit amplifies and filters the induced voltage signal. The processed signal is sent to the channel control module to do the channel control and selection of the signal. And finally use the data processing and display module to carry on the image display, and the calculation of data needs to save. The data can transmit to the host computer, through the communication bus or copy through the SD card. Use the MATLAB functions on the host computer to do the final data processing to determine the locations of all conductors, and guide digging at last.

Considering the actual size of the substation grounding grid, the sensor modules are arranged into an array to improve efficiency of the magnetic field measurement. As shown in Fig. 11, sensor modules are fixed on two PCBs side by side and vertically, to form a $2 \times 8$ sensor array. The horizontal distance between the sensors is 50 mm.

We can measure magnetic field of 16 points each time under this arrangement. Signal from sensor modules is transmitted to the channel control board through RF transmission lines. Sensors are integrated with other modules to form an integrated device as shown in Fig. 12.

The left part in Fig. 12 is the magnetic field sensor module array, and the right side is the combination of other modules. The sensor module array is fixed by the upper and lower PCBs. Nylon pillars are on both sides to support them. On the right, there are the AC excitation current source, power board, and sponge-wrapped lithium battery from top to bottom. There is distance of 5 cm between the boards for heat dissipation. In this device, a piece of silicon steel can be inserted in the middle for electromagnetic shielding to eliminating the interference of function modules.

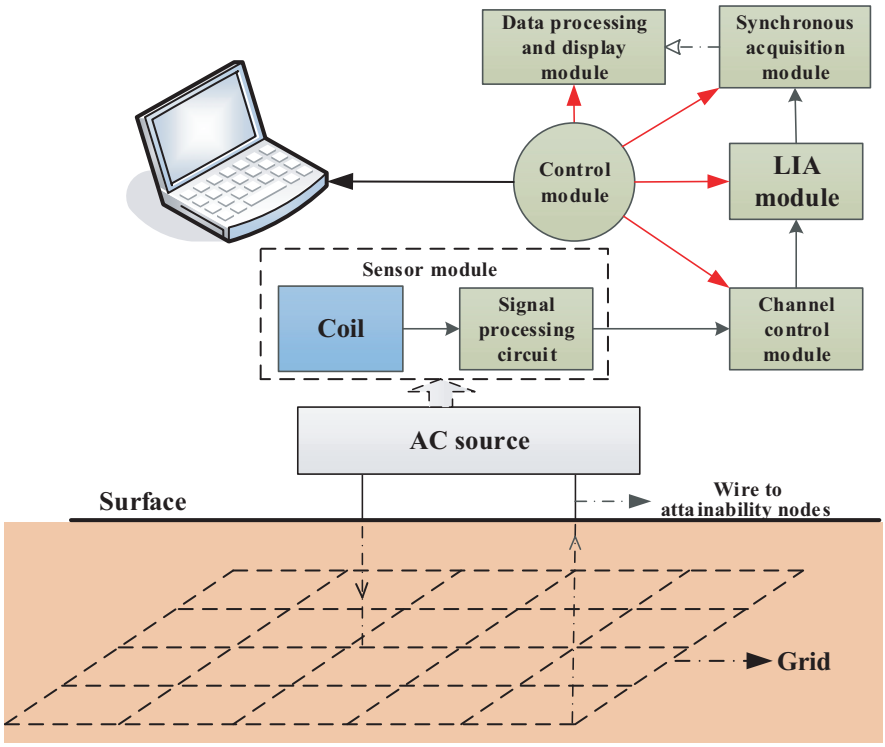


**Figure 10.** The structure of system device.

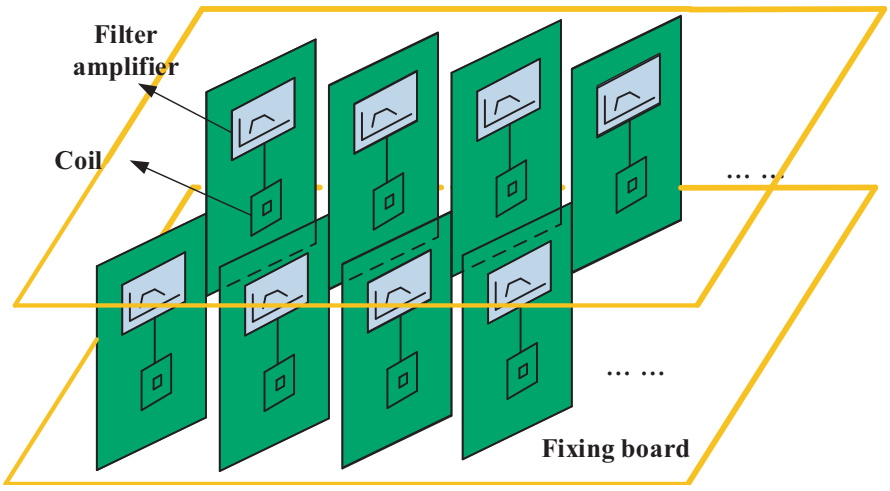


**Figure 11.** Array of magnetic field measurement sensor.

## 5. EXPERIMENTAL ANALYSIS

### 5.1. Single-Conductor Positioning Experiment

For the detection of a single conductor, the detecting device is placed over the conductor and adjust the direction of the device so that the coil PCB is parallel to the line where the conductor is located. The experimental test schematic is shown in Fig. 13. During the measurement, move the detecting device in the direction of the conductor so that a set of magnetic field data perpendicular to the conductor can be obtained. The data are collected by the four-channel synchronous acquisition circuit and uploaded to a portable computer through the serial port to save and display.

**Figure 12.** The whole assembly diagram of device.

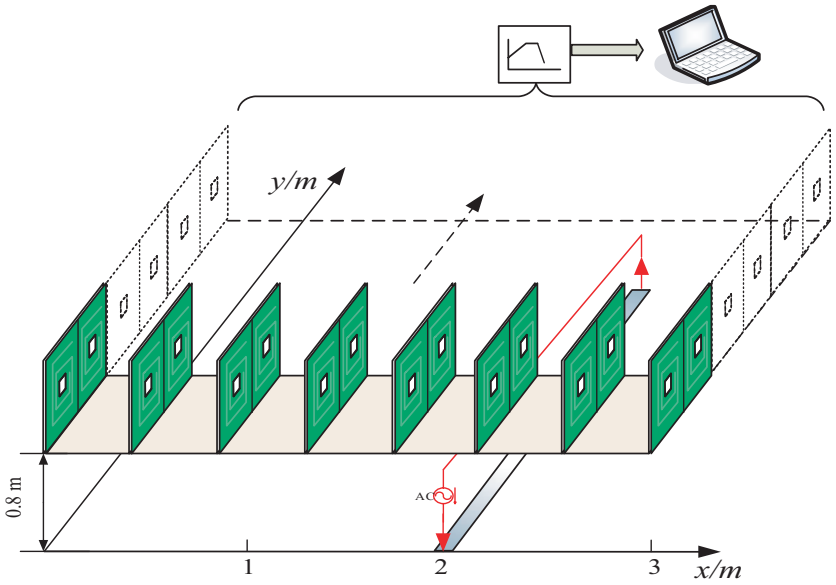


**Figure 13.** The measurement of single conductor.

Five measurements were taken along the $y$-axis, and five sets of data were obtained. Each set of data contains the induced voltage signals measured by the sensor array at 16 points. These induced voltage data are transmitted to computer via serial communication, and the data are converted to the value of magnetic field with *MATLAB* program. The conversion formula is $B_m = v_{om}/k$ as discussed in Section 3 with the conversion factor $k$ of each sensor module being 10000.

Import the converted magnetic field and position data. The gradient of the magnetic field data is calculated by using the center differential function *gradient* in MATLAB. And then draw the graph of magnetic field gradient with position shown in Fig. 14.

The graph shows that a peak is obtained every 5 cm, and the position of the peak is $y = 2.1$ cm. In fact, the position of the flat steel in the experiment is $y = 2$ cm. The measurement error is $\pm 0.1$ cm, and it shows good precision.

### 5.2. Test of Steel Grid Model

In this paper, a scale-down ground grid model made of galvanized flat steel is built to do the test according to the real grounding grid. For the real grounding grid, the cross section of each branch is 60 mm $\times$ 6 mm, and the length is 5 m $\sim$ 15 m. Conductor resistivity is in the order of $10^{-7}\,\Omega \cdot$ m. Take

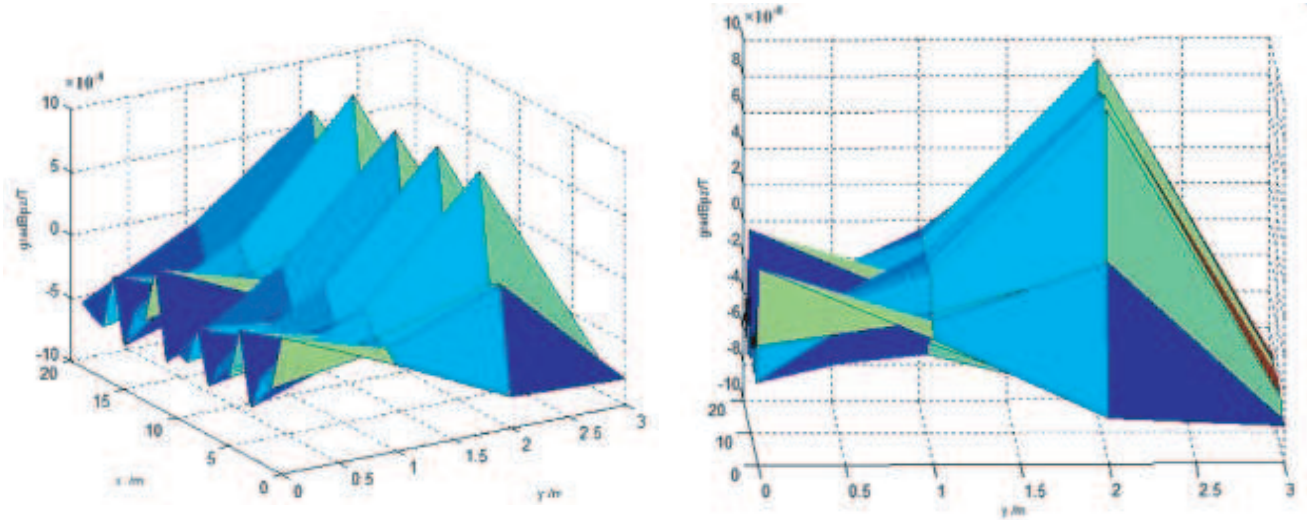

(a) (b)

**Figure 14.** The curve of magnetic field gradient.

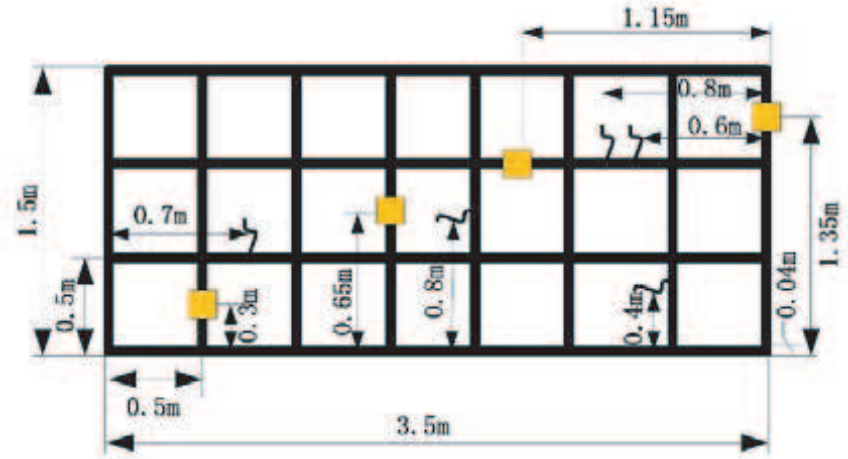


**Figure 15.** The structure of grounding grid f model.

it as $2 \times 10^{-7}\,\Omega \cdot \mathrm{m}$, the resistance of each branch is about $1\,\mathrm{m}\Omega \sim 5\,\mathrm{m}\Omega$. It indicates that the branch resistance is in the order of mΩ. The structure of the galvanized flat steel model is shown in Fig. 15.

Since the network structure of the grounding grid model is known, data can be measured directly in the direction of the branch to verify feasibility. Because of the small size of the flat steel model, it is possible to measure the magnetic flux density of all the areas above the flat steel network at once, and then locate the branches. The results are compared with the actual network structure to test the accuracy of the device.

The method of the measuring and modeling of the model network is explained in Fig. 16. A rectangular space coordinate system is established by taking a vertex of the flat steel network as the origin.

The device measures the magnetic field data 0.6 m above each branch conductor of the grid. After each measurement, move 100 mm forward in the $x$ or $y$ directions, respectively. The procedure is the same as detecting the single conductor. An experimental photo is shown in Fig. 17.

By testing this $7 \times 3$ grid model, the induced voltage data at 0.6 m above the flat steel network can be obtained, to simulate the surface data of buried grid. The induced voltage data are converted to the induced magnetic field data according to the relationship between the induced voltage and the induced

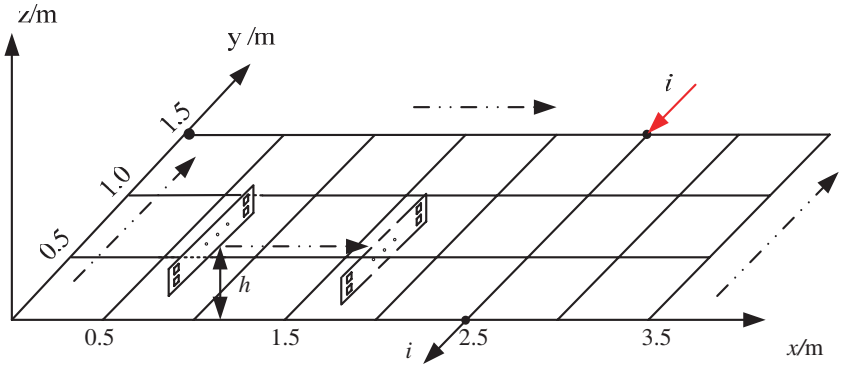


**Figure 16.** The schematic diagram of the measurement.

**Figure 17.** Test of steel grid model.

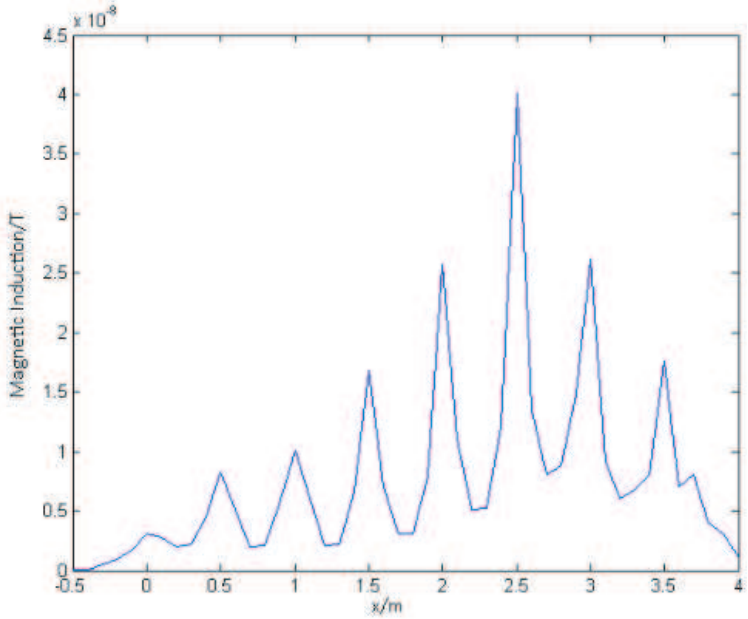


**Figure 18.** The magnetic field above the conductor along $y$ =0.

magnetic field.

Select a branch along the $x$ axis to analyze its magnetic field measurement data, and draw the curve of $\mathbf{B}$ on position. For the sake of generality, select the branch located along $y = 0$ for calculation and plotting. Fig. 18 shows the $B_x(y)$ curve after processing.

From Fig. 18, it can be seen that there are peaks at $x = 0$, $x = 0.5$, $x = 1.0$, $x = 1.5$, $x = 2$, $x = 2.5$, $x = 3$ and $x = 3.5$. According to the conclusion of magnetic field characters in Section 2, there should be a flat steel network branch conductor under these positions. In fact, there are indeed lateral branches at these locations.

## 6. CONCLUSION

By injecting the AC excitation current into the grounding grid, measuring the magnitude of the induced magnetic field above it and drawing the magnetic-position curve, the buried position of the conductor can be judged according to the main peak character. The method works well with different measurement paths. Based on this method, the detecting device can realize the positioning of the grounding grid conductor before excavation and has the advantages of anti-interference ability, high precision and portability. It can provide the convenience for the corrosion diagnosis and digging of grounding grid.

## ACKNOWLEDGMENT

This work was supported by the State Grid Henan Electric Power Corporation Research Institute, China, the State Key Laboratory of Power Transmission Equipment & System Security and New Technology.

## REFERENCES

1. 80-2013 — IEEE Guide for Safety in AC Substation Grounding, 2015.
2. Syrett, B. C. and J. A. Gorman, "Cost of corrosion in the electric power industry: An update," *Materials Performance*, Vol. 42, 7, 2003.
3. Gouda. O. and A. Mohamed, "Ground Potential Rise (GPR) of faulty substations having equal and unequal spacing grounding grids conductors," *IET Generation Transmission & Distribution*, Vol. 11, No. 1, 18–26, 2017.
4. Gillies, D. A., J. D. Randolph, H. Abdallah, and R. S. Brown, "Current north american assessment and refurbishment practices of substation grounding systems," *IEEE Transactions on Power Delivery*, Vol. 20, 1886–1889, 2005.
5. Ramalho, L., W. Rocha, A. Nakamura, B. Arajo, A. Castro, A. Klautau, R. Lima, and R. Freire, "Data acquisition system for continuous monitoring of grounding grids in energized substations," *International Symposium on Instrumentation Systems Circuits and Transducers*, 113–117, 2016.
6. Charalambous, C., N. Kokkinos, and A. Demetriou, "Impact of photovoltaic oriented DC stray current corrosion on large scale solar farms' grounding and third-party infrastructure: Modelling and assessment," *IEEE Transactions on Industry Applications*, Vol. 51, 5421–5430, 2015.
7. Du, J., J. Han, and W. Liu, "The research of grounding grid corrosion factors based on vector similarity and fuzzy techniques," *International Symposium on Computer Consumer and Control*, 625–629, 2014.
8. Colominas, I., J. Gómez-Calviño, F. Navarrina, and M. Casteleiro, "Computer analysis of earthing systems in horizontally or vertically layered soils," *Electric Power Systems Research*, Vol. 59, 149–156, 2001.
9. Habjanic, A., M. Trlep, and J. Pihler, "The influence of an additional substance in the trenches surrounding the grounding grid's conductors on the grounding grid's performance," *IEEE Transactions on Magnetics*, Vol. 43, 1257–1260, 2007.
10. Liu, K, F. Yang, X. Wang, et al., "A novel resistance network node potential measurement method and application in grounding grids corrosion diagnosis," *Progress In Electromagnetics Research M*, Vol. 52, 9–20, 2016.

11. Wang, X., W. He, F. Yang, L. Zhu, and X. Liu, "Topology detection of grounding grids based on derivative method," *Diangong Jishu Xuebao/Transactions of China Electrotechnical Society*, Vol. 30, 73–78, 2015.
12. Li, C., W. He, D. Yao, F. Yang, X. Kou, and X. Wang, "Topological measurement and characterization of substation grounding grids based on derivative method," *International Journal of Electrical Power & Energy Systems*, Vol. 63, 158–164, 2014.
13. C37.235-2007 — IEEE Guide for the Application of Rogowski Coils Used for Protective Relaying Purposes, 2008.
14. Zhang, Y. F., Y. Q. Zhou, X. Yang, and H. B. Hu, "The research and design of electronic current transformer based on PCB planar-type of air core coil," *Asia-Pacific Power and Energy Engineering Conference*, 1–4, 2012.